



# CHORUS

This is the accepted manuscript made available via CHORUS. The article has been published as:

## Lattice dynamics of the hybrid improper ferroelectrics (Ca,Sr)<sub>3</sub>Ti<sub>2</sub>O<sub>7</sub>

Dipanshu Bansal, Jennifer L. Niedziela, Xing He, Tyson Lanigan-Atkins, Ayman Said, Ahmet Alatas, Douglas L. Abernathy, Yang Ren, Bin Gao, Sang-Wook Cheong, and Olivier Delaire

Phys. Rev. B **100**, 214304 — Published 6 December 2019

DOI: [10.1103/PhysRevB.100.214304](https://doi.org/10.1103/PhysRevB.100.214304)

# Lattice dynamics of hybrid improper ferroelectrics $(\text{Ca}, \text{Sr})_3\text{Ti}_2\text{O}_7$

Dipanshu Bansal<sup>1</sup>, Jennifer L. Niedziela<sup>2</sup>, Xing He<sup>1</sup>, Tyson Lanigan-Atkins<sup>1</sup>, Ayman Said<sup>3</sup>, Ahmet Alatas<sup>3</sup>, Douglas L. Abernathy<sup>4</sup>, Yang Ren<sup>3</sup>, Bin Gao<sup>5</sup>, Sang-Wook Cheong<sup>5</sup>, and Olivier Delaire<sup>1</sup>

<sup>1</sup>*Mechanical Engineering and Materials Science, Duke University, Durham, North Carolina 27708, USA*

<sup>2</sup>*Materials Science and Technology Division, Oak Ridge National Laboratory, Oak Ridge, Tennessee 37831, USA*

<sup>3</sup>*Advanced Photon Source, Argonne National Laboratory, Argonne, Illinois 60439, USA*

<sup>4</sup>*Neutron Scattering Division, Oak Ridge National Laboratory, Oak Ridge, Tennessee 37831, USA*

<sup>5</sup>*Rutgers Center for Emergent Materials and Department of Physics & Astronomy,*

*Rutgers University, Piscataway, New Jersey 08854, USA*

(Dated: November 21, 2019)

The structure and lattice dynamics of the hybrid improper ferroelectric compound  $\text{Ca}_{3-x}\text{Sr}_x\text{Ti}_2\text{O}_7$  (for  $x = 0, 0.6$ , and  $0.9$ ) have been studied with a combination of diffraction, inelastic scattering experiments, Raman spectroscopy and calorimetry measurements, as well as first-principles simulations. Using inelastic neutron scattering (INS), we have measured the phonon density of states (DOS) for  $x = 0.9$ , which revealed a strong broadening but little change in phonon energies on heating from 10 K to 728 K across the ferroelectric phase transition temperature,  $T_{FE}$ . Using inelastic x-ray scattering (IXS), the momentum-resolved phonon dispersions were measured from 80 K to 950 K on a single-crystal (for  $x = 0.6$ ), and also revealed a strong phonon broadening but a small energy shift for acoustic modes on heating across  $T_{FE}$ . Our Raman measurements (for  $x = 0.6$ ) showed robust rotational and oxygen breathing modes but soft tilt modes, consistent with previous measurements on similar compounds. Our density functional calculations achieve good agreement with both the phonon DOS and dispersions measured. We did not observe any unusual quadratic dispersion for  $c$ -polarized transverse acoustic modes, at odds with a recently predicted quasi-2D character, for either undoped ( $x = 0$ ) or doped ( $x = 0.6$ ) compounds.

## I. INTRODUCTION

Multiferroics exhibit coexisting, spontaneous switchable ferroelectric polarization  $P$  and magnetization  $M$ . Some of the possible mechanisms enabling ferroelectric order include stereochemically active lone-pairs, geometric ferroelectricity, charge ordering, and spin-driven ferroelectricity [1]. In particular, geometric ferroelectrics – improper and hybrid-improper – have attracted intense interest because of unique domain topology [2–5] and the control of a polar distortion via instabilities of non-polar modes, circumventing the natural incompatibility of displacive ferroelectrics with magnetism associated with their empty transition metal  $d$  orbitals [1, 6–8].

The compounds  $\text{Ca}_3\text{Ti}_2\text{O}_7$  and  $\text{Ca}_3\text{Mn}_2\text{O}_7$ , among the simplest Ruddlesden-Popper (RP) structures ( $A_{n+1}B_nO_{3n+1}$ ), were theoretically predicted to host hybrid-improper ferroelectricity [9]. In these compounds, it was proposed that two unstable zone-boundary modes couple with a stable zone-center polar mode to yield the non-centrosymmetric phase with emergent polarization [9]. While the spontaneous and switchable  $P$  has been experimentally demonstrated in the RP structures [10], their lattice dynamics across the ferroelectric transition temperature ( $T_{FE}$ ) have remained little explored. In particular, experimental measurements of phonon dispersions of  $\text{Ca}_3\text{Ti}_2\text{O}_7$ , which are critical to assess the proposed improper anharmonic coupling mechanism, have not yet been reported, to our knowledge.

Recently, neutron and x-ray diffraction measurements on single-crystals of  $\text{Ca}_3\text{Mn}_{1.9}\text{Ti}_{0.1}\text{O}_7$  revealed robust-

ness and softness of static amplitude of the in-plane rotation mode and the out-of-plane antiphase tilt mode, respectively [11]. A similar conclusion was drawn from Raman scattering measurements on  $\text{Ca}_3\text{Mn}_2\text{O}_7$  that showed relatively small phonon energy change for the rotational mode in comparison to the tilt mode below  $T_{FE}$  [12]. However, we note that in  $\text{Ca}_3\text{Mn}_{2-x}\text{Ti}_x\text{O}_7$ , the Mn ions order antiferromagnetically (moment dominantly pointing along the  $c$ -axis) below  $T_N < 115\text{ K}$  [11], thus introducing a spin degree of freedom in the temperature dependence of the rotation and tilt distortions. Besides, there are marked differences in the  $d$ -orbital occupation of Mn and Ti compounds with  $\text{Mn}^{4+}$  being partially occupied, while  $\text{Ti}^{4+}$  has empty  $d$ -orbitals. Based on density functional theory (DFT) simulations, the partial occupation of  $d$ -orbitals was shown to increase the amplitude of static antiphase tilt in  $\text{Ca}_3\text{Mn}_2\text{O}_7$ , while keeping the static rotation amplitude unchanged i.e., robust under pressure [11]. However, for empty  $d$ -orbitals, enhanced hopping between O- $2p$  and Ti- $3d$  was theoretically predicted to increase both the static rotation and tilt [11, 13].

Moreover, a recent first-principles study of lattice dynamics has identified quasi-two-dimensional vibrations in  $(\text{Ca}, \text{Sr})_3(\text{Zr}, \text{Ti})_2\text{O}_7$ , based on unusual quadratic dispersion of  $c$ -polarized transverse acoustic modes propagating along  $[H, 0, 0]$  ( $\text{TA}_c^{[H00]}$ ) [14]. This branch was shown to be very sensitive to volume changes in  $\text{Ca}_3\text{Ti}_2\text{O}_7$ , with Grüneisen parameters exceeding 25 near the zone-center. Since this TA mode and the transverse optical (TO) mode along the same direction were identified as responsible for the tunable negative thermal expansion

with pressure, it is critical to verify the quasi-2D character of the TA mode experimentally.

Here, we present a detailed investigation of the lattice dynamics of  $(\text{Ca}, \text{Sr})_3\text{Ti}_2\text{O}_7$ , based on inelastic x-ray scattering (IXS), inelastic neutron scattering (INS) and Raman spectroscopy, combined with DFT simulations. We have measured the phonon energies and linewidths across the Brillouin zone, for varying temperatures encompassing  $T_{FE}$ . In addition, we performed single-crystal diffraction and calorimetry measurements to characterize the ferroelectric transition. We find the phase transition to be first-order with a hysteresis of about 30 K ( $x = 0.6$ ), consistent with previous diffraction and calorimetry results on  $\text{Ca}_3(\text{Mn}, \text{Ti})_2\text{O}_7$  [11, 15] and  $(\text{Ca}, \text{Sr})_3\text{Ti}_2\text{O}_7$  [16]. Powder INS measurements on  $\text{Ca}_{2.1}\text{Sr}_{0.9}\text{Ti}_2\text{O}_7$  show a significant broadening of both low and high energy phonon modes on heating from 10 to 728 K, suggesting the presence of strong anharmonicity. We observe only a small change in the phonon density of states across  $T_{FE}$ . Single-crystal IXS measurements on  $\text{Ca}_{2.4}\text{Sr}_{0.6}\text{Ti}_2\text{O}_7$  also showed a small change in the phonon energy ( $<1$  meV) of acoustic modes in heating across  $T_{FE} \sim 750$  K from 300 to 900 K. However, we observe a substantial phonon broadening (by a factor of  $\sim 2$ ) of acoustic modes in the same temperature range, based on IXS. Our INS measurements also reveal a strong broadening of the DOS across the frequency spectrum. In our IXS measurements, the  $\text{TA}_c^{[H00]}$  branch did not exhibit quasi-2D character, contrary to first-principles simulations of Huang *et al.* [14], and had a negative thermal Grüneisen parameter for  $H \leq 0.3$  (phonon energy increasing on warming). Our Raman measurements on  $\text{Ca}_{2.4}\text{Sr}_{0.6}\text{Ti}_2\text{O}_7$  revealed pronounced softening of the soft tilt mode but a robust rotational mode, similar to previous results on related compounds with partially occupied Mn *d*-orbitals. Surprisingly, oxygen breathing modes (corresponding to each perovskite layer moving against each other along the *c*-axis) showed a softening of less than 0.5 meV between 300 and 1023 K remaining stiff even at the highest temperature measured.

## II. EXPERIMENTS

### A. Sample Preparation

Polycrystalline specimens of  $\text{Ca}_{3-x}\text{Sr}_x\text{Ti}_2\text{O}_7$  ( $x = 0.9$ ) were prepared using a solid-state reaction method. Stoichiometric mixtures of  $\text{CaCO}_3$  (Alfa Aesar 99.95%),  $\text{SrCO}_3$  (Alfa Aesar 99.99%) and  $\text{TiO}_2$  (Alfa Aesar Puratronic 99.995%) powders were ground, pelletized and subsequently sintered at 1550–1600°C for 30 h. Single-crystals ( $x = 0, 0.6$ ) were grown by an optical floating zone method, as described previously [10].

### B. Inelastic Neutron Scattering

Inelastic neutron scattering (INS) measurements on a powder sample of  $\text{Ca}_{2.1}\text{Sr}_{0.9}\text{Ti}_2\text{O}_7$  were carried out using the time-of-flight wide angular-range chopper spectrometer (ARCS) at the Spallation Neutron Source (SNS) at Oak Ridge National Laboratory [17]. The powder (mass  $\sim 9.4$  g) was encased in a thin-walled aluminum can. We used a closed-cycle helium refrigerator for measurements at low temperature ( $10 \leq T \leq 300$  K), and a low-background resistive furnace for high temperature measurements ( $300 < T \leq 728$  K). Two incident neutron energies  $E_i = 70$ , and 140 meV were used at each temperature to probe the full spectrum of oxygen vibrations up to 110 meV ( $E_i = 140$  meV) while maintaining good resolution on lower-energy modes involving Ca and Ti (70 meV). The empty aluminum can was measured in identical conditions at all temperatures. The energy resolution (full width at half maximum) for incident energies  $E_i = 70$ , and 140 meV is  $\sim 2.6$ , and 7.5 meV at the elastic line, respectively, which reduces to 1.3 and 5.3 meV, respectively at an energy transfer of 40 meV.

The measured counts were transformed from instrument coordinates, scattering angle and neutron detection times, to the dynamical structure factor  $S(|Q|, E)$  as function of momentum transfer,  $|Q|$ , and energy transfer,  $E$ , using the MANTID software [18]. Subsequently, two-dimensional intensity maps for the dynamical susceptibility,  $\chi''(|Q|, E) = (1 - \exp(-E/k_B T))S(|Q|, E)$ , were calculated from  $S(|Q|, E)$ . The phonon density of states (DOS) was obtained from data collected with  $E_i = 140$  meV by integrating over the entire  $|Q|$  range, and applying corrections for background and multi-phonon scattering, and removing the elastic peak as described in our earlier work [19].

The phonon spectra from INS measurements are weighted by the relative neutron scattering strengths ( $\sigma/m$ ) of the elements in the sample, where  $\sigma$  is the total neutron scattering cross-section, and  $m$  the atomic mass. The neutron-weighting (NW) factors for Ca, Sr, Ti, and O are  $\sigma_{Ca}/m_{Ca} = 0.0706$ ,  $\sigma_{Sr}/m_{Sr} = 0.0713$ ,  $\sigma_{Ti}/m_{Ti} = 0.0909$ , and  $\sigma_O/m_O = 0.2645$ , respectively (in units of barns/amu). Consequently, the neutron-weighted (NW) phonon DOS measured with INS,  $g_{NW}(E)$ , for  $\text{Ca}_{2.1}\text{Sr}_{0.9}\text{Ti}_2\text{O}_7$  is over-weighted for the Ti and O vibrational contributions:

$$g_{NW}(E) = \left( \sum_i \frac{x_i \sigma_i g_i(E)}{m_i} \right) / \left( \sum_i \frac{x_i \sigma_i}{m_i} \right) \quad (1)$$

where  $g_i$  are the partial DOS of atoms  $i = \text{Ca}, \text{Sr}, \text{Ti}$ , and O, respectively,  $x_i$  the atomic fraction. The resulting NW phonon DOS is normalized to a unit area and can be directly compared against the simulated DOS to which the same neutron weights are applied.

### C. Single-Crystal Inelastic X-ray Scattering

We used high-resolution inelastic x-ray scattering (IXS) to measure phonon dispersion curves of  $\text{Ca}_{3-x}\text{Sr}_x\text{Ti}_2\text{O}_7$  ( $x = 0$  and  $0.6$ ) on small single crystals of approximately  $\sim 0.5 \times 0.4 \times 0.06 \text{ mm}^3$  from  $T = 70$  to  $900 \text{ K}$ . The mosaic of the samples was less than  $0.06^\circ$  and  $0.035^\circ$  for the in- and out-of-plane Bragg peaks. The experiments were conducted at beamline 30-ID-C (HERIX [20, 21]) at the Advanced Photon Source (APS). The highly monochromatic x-ray beam had an incident energy  $E_i \simeq 23.7 \text{ keV}$  ( $\lambda = 0.5226 \text{ \AA}$ ) and an energy resolution  $\Delta E_i \sim 1.0 \text{ meV}$  (full width at half maximum), and was focused on the sample to a cross-section  $\sim 35 \times 15 \text{ }\mu\text{m}$  (horizontal  $\times$  vertical). The convoluted energy resolution of the incident x-ray beam and analyzer crystals was  $\Delta E \sim 1.32 \text{ meV}$  and can be approximated as Gaussian function for all phonon energies [19, 22]. The crystal was glued to a copper post using Ag paste and mounted in a high-temperature vacuum furnace. The measurements were performed in the transmission geometry. Typical counting times were 40 to 120 s at each point in the energy scans at constant  $Q$ .

The orientation matrix was defined using (2,2,0) and (0,0,-10) Bragg peaks, and checked with other peaks. The longitudinal and transverse acoustic dispersions were measured along high symmetry directions  $(\xi, 0, -10)$ ,  $(0, \xi, -10)$ ,  $(\xi, 4, 0)$ ,  $(0, 4, \xi)$ ,  $(\xi, \xi, -10)$ ,  $(0, \xi, 0)$ ,  $(2 + \xi, 2 - \xi, 0)$ ,  $(2 + \xi, 2 + \xi, 0)$ , and  $(0, \xi, -10 + 3\xi)$ . The measured spectra were fitted with a set of damped-harmonic-oscillator (DHO) scattering functions [23],  $S_{\text{DHO}}(E)$ , subsequently convoluted with the measured instrumental resolution function  $R(E)$ :

$$S_{\text{DHO}}(E) = A \sum_i \frac{\{\frac{1}{2} \pm \frac{1}{2} + n(|E|)\} \times \Gamma_i E}{(E^2 - E_i^2)^2 + (\Gamma_i E)^2} + B, \quad (2)$$

where  $B$  is a constant background,  $n(E)$  is the temperature-dependent Bose-Einstein distribution at energy transfer  $E$ ,  $A$  is the amplitude,  $\Gamma_i$  is the full width at half maximum of the phonon peak  $i$ , and  $E_i$  its renormalized phonon energy in the presence of damping (the + sign is for  $E > 0$  and the - sign for  $E < 0$ ).

### D. Raman Scattering

Raman measurements were performed using a HORIBA T64000 spectrometer in a triple-subtractive mode on a randomly oriented single-crystal sample of  $\text{Ca}_{2.4}\text{Sr}_{0.6}\text{Ti}_2\text{O}_7$  with dimensions  $1 \times 1 \times 0.1 \text{ mm}^3$  in a Linkam TS1500 stage at  $T = 303 \text{ K}$  and from  $373$  to  $1023 \text{ K}$  in steps of  $50 \text{ K}$  (the measurement at  $294 \text{ K}$  was in open environment). The incoming beam from a Nd:YAG laser ( $\lambda = 532 \text{ nm}$ , power =  $6 \text{ mW}$  at sample) was parallel to the  $c$  axis, and spectra were collected in backscattering geometry. The measured temperature on the sample position was calibrated using the Raman peak

at  $418 \text{ cm}^{-1}$  [24] of a sapphire disk placed underneath the sample. The low laser power minimized local heating.

### E. Single-Crystal X-ray Diffraction

Single-crystal x-ray diffraction (XRD) was performed on a  $5 \times 5 \times 1 \text{ mm}^3$  crystal of  $\text{Ca}_{2.4}\text{Sr}_{0.6}\text{Ti}_2\text{O}_7$  with hard X-rays ( $E_i = 105.091 \text{ keV}$ ) at beamline 11-ID-C at the Advanced Photon Source from  $T = 343$  to  $873 \text{ K}$ . The crystal was mounted in a Linkam TS1500 stage in  $[H, K, 0]$  scattering plane. The x-ray beam dimensions were  $0.2 \times 0.2 \text{ mm}^2$ . Argon gas was continuously flown around the sample.

### F. Calorimetry

Differential scanning calorimetry measurements were performed with a Netzsch DSC 404 F1 Pegasus, with the  $\text{Ca}_{2.4}\text{Sr}_{0.6}\text{Ti}_2\text{O}_7$  sample loaded inside a Pt crucible, under an ultra-pure Ar purge gas cycled through a Ti gettering furnace. The scans were performed after careful evacuation and purging of the sample chamber. The heating rate was  $10 \text{ K/min}$ . The sample mass was  $22.3 \text{ mg}$ .

## III. DENSITY FUNCTIONAL THEORY SIMULATIONS

First-principles simulations were performed in the framework of density functional theory (DFT) as implemented in the Vienna *Ab initio* Simulation Package (VASP 5.3) [25–27]. A  $6 \times 6 \times 2$  Monkhorst-Pack electronic  $k$ -point mesh with a plane-wave cut-off energy of  $600 \text{ eV}$  and energy convergence threshold of  $10^{-8} \text{ eV}$  were used in all simulations. The projector-augmented-wave potentials explicitly included  $3s^2 3p^6 4s^2$ ,  $3p^6 3d^2 4s^2$ , and  $2s^2 2p^4$  valence configuration for Ca, Ti, and O, respectively. We used the generalized gradient approximation (GGA) in the PBEsol parametrization [28].

During the relaxation of the structure, the lattice parameters and atomic positions were optimized until forces on all atoms were smaller than  $1 \text{ meV \AA}^{-1}$ . The relaxed lattice parameters ( $a = 5.387 \text{ \AA}$ ,  $b = 5.440$ ,  $c = 19.305 \text{ \AA}$ ) differed from our IXS experimental values of  $\text{Ca}_3\text{Ti}_2\text{O}_7$  measured at  $300 \text{ K}$  ( $a = 5.422 \text{ \AA}$ ,  $b = 5.423 \text{ \AA}$ ,  $c = 19.528 \text{ \AA}$ ) less than  $1.1\%$  along the  $c$  and  $0.7\%$  along the  $a$  axis. Calculations of phonon dispersions were performed in the harmonic approximation, using the finite displacement approach as implemented in Phonopy [29], using the atomic forces obtained with VASP. The phonon calculations used a  $2 \times 2 \times 1$  supercell of the orthorhombic cell containing 192 atoms. To construct the force-constant matrix using the finite displacement approach, 38 independent atomic displacements were computed. The atomic displacement amplitude was  $0.01 \text{ \AA}$ . Simulations were also carried out by changing the lattice parameters

by  $\pm 1\%$ , and constructing the force-constants matrix after relaxation of the atomic positions. The simulated phonon dispersions and phonon DOS showed reasonable agreement with IXS and INS measurements for the compressed unit cell ( $-1\%$  change in lattice parameters), as shown below. We note, however, that our phonon simulations with the relaxed lattice parameters showed a quadratic curvature for  $\text{TA}_c^{[H00]}$  and  $\text{TA}_c^{[HH0]}$  branches, similar to that reported in Ref. 14, which disagrees with our IXS measurements. Phonons are very sensitive to volume in this system, which is characteristic of anharmonic materials near lattice instabilities, and also illustrates limitations of quasi-harmonic phonon theory.

Raman scattering intensity simulation were performed using the same relaxed cell as described above. The Raman intensity  $I_s$  of the  $j$ -th phonon mode with frequency  $\omega_j$  is given by [30, 31]:

$$I_s = \frac{d\sigma}{d\Omega} = N_c \frac{\omega_s^4}{c^4 V} |\mathbf{g}_s \cdot \boldsymbol{\alpha}(j) \cdot \mathbf{g}_i^T|^2 \frac{\hbar}{2\omega_j} (n(\omega_j) + 1), \quad (3)$$

where

$$\alpha_{mn}(j) = V \sum_{\mu=1}^N \sum_{l=1}^3 \frac{\partial \chi_{mn}}{\partial r^l(\mu)} \frac{e_{\mu}^l(j)}{\sqrt{M_{\mu}}}, \quad (4)$$

and  $N_c$  is the number of unit cells in the sample,  $\omega_s = \omega_i \pm \omega_j$  (plus and minus signs are anti-stokes and Stokes process),  $\omega_i$  is the frequency of incoming light,  $V$  is the volume of unit cell,  $c$  is the speed of light,  $n(\omega_j)$  is the Bose-Einstein factor of the  $j$ -th mode,  $\mathbf{g}_s$  and  $\mathbf{g}_i$  are polarization vectors of the scattered and incoming light,  $\hbar$  the reduced Planck constant,  $\chi_{mn} = (\epsilon_{mn} - \delta_{mn})$  is the electric polarizability tensor specified in terms of the macroscopic dielectric tensor  $\epsilon_{mn}$ ,  $r^l(\mu)$  and  $e_{\mu}^l(j)$  are the position and eigenvector of the  $\mu$ -th atom along the direction  $l$ , and  $M_{\mu}$  is the mass of the  $\mu$ -th atom. Combining Eq. (3) and (4) and averaging over all orientations and assuming the Raman susceptibility  $\boldsymbol{\alpha}$  to be symmetric, we can calculate the Raman intensity of a polycrystalline sample,  $I_{pc}$  as follows [30]:

$$I_{pc} \propto [10G_i^{(0)} + 7G_i^{(2)}]. \quad (5)$$

Here,

$$G_i^{(0)} = \frac{1}{3} (\alpha_{xx} + \alpha_{yy} + \alpha_{zz})^2, \quad \text{and} \quad (6)$$

$$G_i^{(2)} = 2 [\alpha_{xy}^2 + \alpha_{xz}^2 + \alpha_{yz}^2] \quad (7)$$

$$+ \frac{1}{3} [(\alpha_{xx} - \alpha_{yy})^2 + (\alpha_{yy} - \alpha_{zz})^2 + (\alpha_{zz} - \alpha_{xx})^2]. \quad (8)$$

The phonon frequency  $\omega_j$  and eigenvector  $e_{\mu}^l(j)$  of the  $j$ -th mode at the  $\Gamma$  point and the macroscopic dielectric tensor were calculated using density functional perturbation theory as implemented in VASP. The first derivative of the electric polarizability tensor, i.e.,  $\alpha_{mn}$ , was evaluated by displacing the atoms by mass-normalized phonon eigenvectors around minima in both directions and determining the change in the macroscopic dielectric tensor.

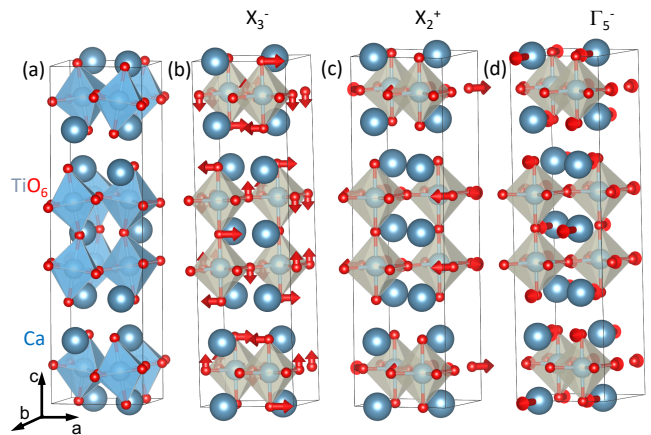


FIG. 1. (a)  $\text{Ca}_3\text{Ti}_2\text{O}_7$  crystal structure in the low-temperature  $A2_1am$  (space group 36) polar phase showing the rotation and tilt of  $\text{TiO}_6$  polyhedra and in-plane displacement of  $\text{Ca}$  ions. (b-d) Decomposition of the total distortion into the symmetry adapted modes  $X_3^-$  (tilt),  $X_2^+$  (in-plane rotation), and  $\Gamma_5^-$  modes of the high-temperature  $I4/mmm$  (space group 139) structure.

## IV. RESULTS

The RP compounds  $A_{n+1}B_n\text{O}_{3n+1}$ , where  $A = \text{Ca, Sr, La}$  and  $B = \text{Ti, Mn, Fe, V, Ru, Ir}$ , can be seen as stackings of  $n$  slabs of the perovskite structure ( $ABO_3$ ) separated by single  $AO$  rock-salt layers along the  $c$ -axis. They display interesting physical properties including multiferroicity [9, 32, 33]. The ( $n = 2$ ) RP structures  $\text{Ca}_{3-x}\text{Sr}_x\text{Ti}_2\text{O}_7$  ( $x = 0, 0.6, 0.9$ ) studied here crystallize in a non-polar tetragonal phase  $I4/mmm$  at high-temperature and undergo a ferroelectric transition to a polar orthorhombic phase  $A2_1am$  on cooling below  $T_{FE}$  for  $x \leq 0.6$ , and possibly go through an intermediate non-polar tetragonal phase ( $P4_2/mmm$ ) for  $0.6 < x \leq 0.9$  [34]. Figure 1 shows both the high- and low-temperature crystal structures of  $\text{Ca}_3\text{Ti}_2\text{O}_7$  along with rotation and tilt patterns of  $\text{TiO}_6$  polyhedra. The arrows in Fig. 1(b-d) represent the structural distortion between the two phases ( $I4/mmm$  and  $A2_1am$  for  $x \leq 0.6$ ), decomposed into symmetry adapted modes of the high-temperature phase:  $X_3^-$  (tilt),  $X_2^+$  (in-plane rotation), and  $\Gamma_5^-$  (polar mode), obtained using group theoretical analysis [9, 35, 36]. Here, the  $\Gamma$  and  $X$  points refer to  $(0,0,0)$  and  $(\frac{1}{2}, \frac{1}{2}, 0)$  points in the Brillouin zone of the high-temperature phase.

### A. Calorimetry and diffraction

Our calorimetry measurements for  $x = 0.6$  clearly reveal the ferroelectric transition at  $\sim 751$  K and  $\sim 719$  K on heating and cooling, respectively, as shown in Fig. 2a. The hysteresis of nearly 30 K suggests that the transi-

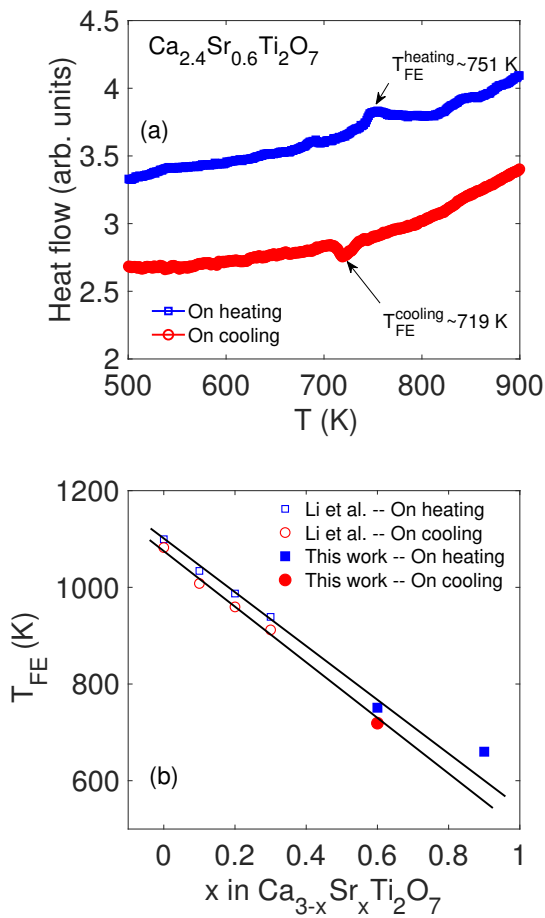


FIG. 2. (a) Heat flow measurements of  $\text{Ca}_{2.4}\text{Sr}_{0.6}\text{Ti}_2\text{O}_7$  sample across  $T_{FE}$  on heating and cooling showing the transition at 751 and 719 K, respectively. (b) Ferroelectric transition temperature  $T_{FE}$  as a function of ‘ $x$ ’ in  $\text{Ca}_{3-x}\text{Sr}_x\text{Ti}_2\text{O}_7$  from Li *et al.* [16] and from the present study showing nearly linear decrease with increasing ‘ $x$ ’.

tion is of first-order, consistent with previous diffraction and calorimetry measurements for different  $x$  values, as well as in other related RP compounds [11, 15, 16]. Our results are consistent with and extend the linearly decrease of  $T_{FE}$  with increasing  $x$  reported in [16], as shown in Fig. 2b (the deviation for  $x = 0.9$  could be due to the presence of an intermediate non-polar phase [34]). Our single-crystal XRD measurements on the same composition in [HK0] scattering plane further also confirm the structural phase transition. Figure 3(a,c) shows the x-ray scattering intensity at 343 and 873 K respectively, below and above  $T_{FE} \sim 751$  K. The superlattice peaks, i.e. (2,1,0), emerging below  $T_{FE}$  are marked by black circles. The experimental data are compared with simulated x-ray intensities in panels (b) and (d). We note that in the simulated XRD pattern in (b), superlattice peaks appear at (2,1,0) and not at (1,2,0), but in the experimental data, multiple twin domains in the sample lead to the observation of both (2,1,0) and (1,2,0) peaks. The

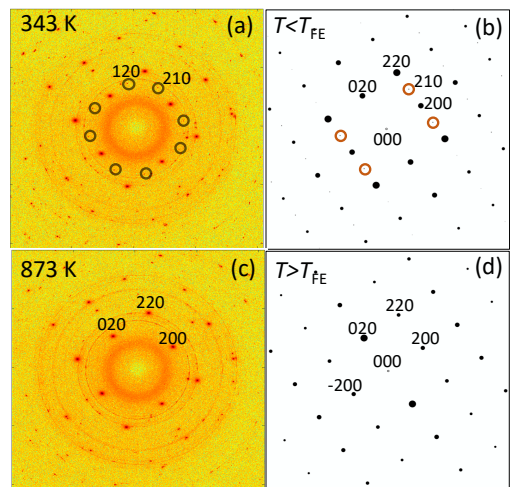


FIG. 3. XRD from a  $\text{Ca}_{2.4}\text{Sr}_{0.6}\text{Ti}_2\text{O}_7$  single-crystal (a) below and (c) above  $T_{FE}$  in the [HK0] scattering plane, and comparison with the respective simulated intensities in panels (b) and (d). In the simulated pattern, the superlattice peaks for  $H = 2n$  and  $K = 2n + 1$  (i.e., 210, 2-10) emerge below  $T_{FE}$ . Experimental data in panel (a) also show the presence of the superlattice peaks for  $H = 2n + 1$  and  $K = 2n$  due to twinning of the sample in the orthorhombic phase. Selected superlattice peaks are circled in panel (a) and (b).

superlattice peak (2,1,0) primarily originates from the  $X_2^+$  distortion, but has a small contribution from the  $X_3^-$  distortion as well. We note that the single-crystal used in our XRD measurements (much larger than the one used for IXS) had some other randomly oriented small grains leading to several weak spots (along rings). However, the sharp diffraction spots of the primary crystal are clearly identified.

## B. INS measurements on polycrystalline $\text{Ca}_{2.1}\text{Sr}_{0.9}\text{Ti}_2\text{O}_7$ sample

We now focus on the atomic dynamics and their evolution across the ferroelectric transition. Figures 4 and 5 show the powder  $S(|Q|, E)$  from INS for  $x = 0.9$  from 10 to 728 K for incident neutron energy  $E_i$  of 70 and 140 meV, respectively. The higher energy resolution with  $E_i = 70$  meV clearly resolves the low energy phonon peaks. The phase transition temperature for this composition was determined to be  $\sim 660$  K from our calorimetry measurements on heating. It is apparent from Fig. 4 and 5 that the phonon intensity at a given temperature increases with increase in  $|Q|$ , as expected from the  $(\mathbf{Q} \cdot \boldsymbol{\epsilon})^2$  dependence ( $\boldsymbol{\epsilon}$  is the phonon eigenvector) of  $S(|Q|, E)$ , and also increases with temperature following the Bose-Einstein occupation factor. The phonons obviously broaden with increasing temperature due to the increased atomic vibrational amplitude and anharmonic effects, which are significant in this system. The

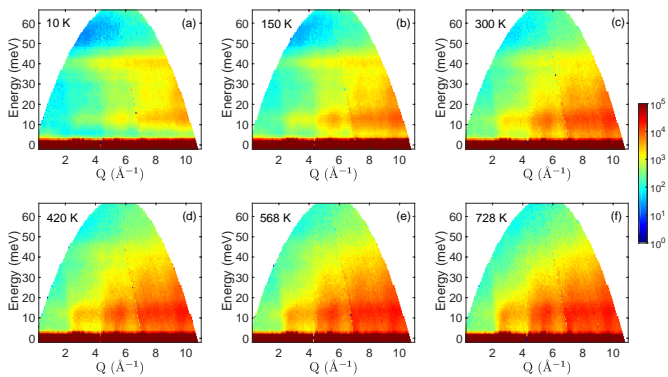


FIG. 4. Dynamical structure factor  $S(|Q|, E)$  of  $\text{Ca}_{2.1}\text{Sr}_{0.9}\text{Ti}_2\text{O}_7$  powder sample at multiple temperatures (indicated on each panel) across  $T_{FE} \sim 660$  K, measured on ARCS with incident neutron energy  $E_i = 70$  meV. The intensity is in log scale.

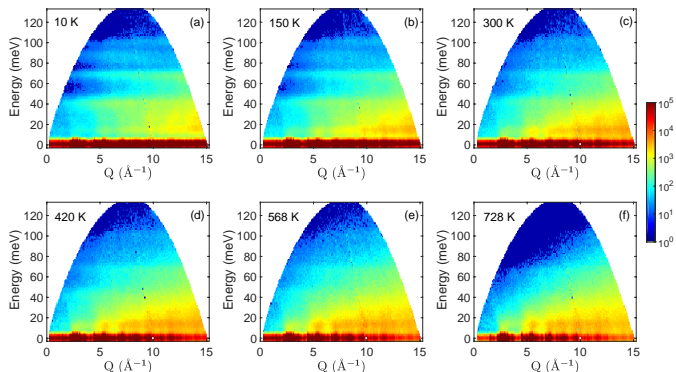


FIG. 5. Dynamical structure factor  $S(|Q|, E)$  of  $\text{Ca}_{2.1}\text{Sr}_{0.9}\text{Ti}_2\text{O}_7$  powder sample at multiple temperatures (indicated on each panel) across  $T_{FE} \sim 660$  K, measured on ARCS with incident neutron energy  $E_i = 140$  meV. The intensity is in log scale.

phonon broadening is also observed in our IXS and Raman measurements (see below). The phonon energy cutoff is around 110 meV as seen in Fig. 5.

We now analyze the 2-D  $S(|Q|, E)$  maps in more detail. Figure 6 shows the dynamical susceptibility  $\chi''(E) = (1 - \exp(-E/k_B T))S(E)$  after  $|Q|$  integration over  $3.5 < |Q| < 7.5$  and  $4.75 < |Q| < 10.75 \text{ \AA}^{-1}$  for  $E_i$  of 70, and 140 meV, respectively. From these spectra, one can observe a significant broadening of phonon features even at low temperatures (e.g. between 10 K and 300 K), for both the low and high energy phonons. The broadening keeps increasing with temperature to 728 K and phonon peaks that are well-defined at low-temperatures merge into a smooth continuum of intensity. Interestingly, despite the ferroelectric transition being first-order in nature, the overall phonon spectrum does not show a clear discontinuity across  $T_{FE} \sim 660$  K. Similar results are observed in our momentum-resolved IXS measurements for

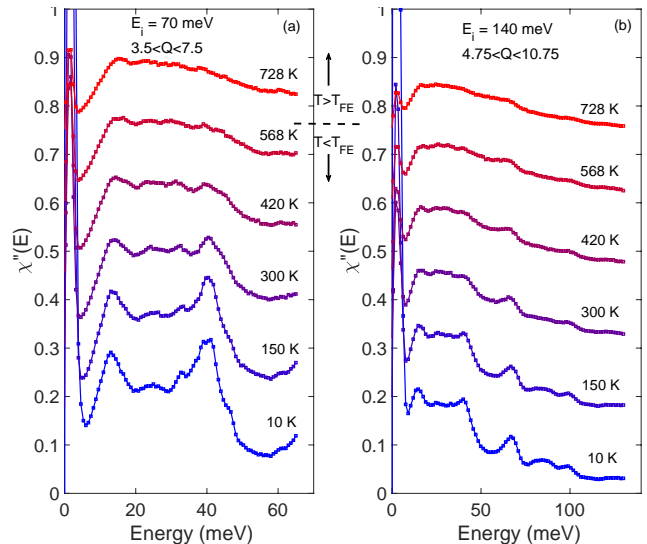


FIG. 6. Dynamical susceptibility  $\chi''(E)$  of  $\text{Ca}_{2.1}\text{Sr}_{0.9}\text{Ti}_2\text{O}_7$  calculated from the dynamical structure factor  $S(E)$  using  $\chi''(E) = (1 - \exp(-E/k_B T))S(E)$  by integrating the data in Fig. 4 and 5 between  $3.5 < |Q| < 7.5$  and  $4.75 < |Q| < 10.75 \text{ \AA}^{-1}$ , respectively, for the incident energy  $E_i$  of (a) 70, and (b) 140 meV. Curves in both the panels are offset by 0.15 for clarity.

$x = 0.6$  composition (see below).

$S(|Q|, E)$  data in Fig. 5 were corrected for background, occupation factor, and multiple and multi-phonon scattering to obtain the phonon DOS (see Section IIB for details). Figure 7 shows the phonon DOS of  $\text{Ca}_{2.1}\text{Sr}_{0.9}\text{Ti}_2\text{O}_7$  from 10 to 728 K. The experimental DOS is compared to our DFT simulations of the total (neutron-weighted) and partial DOS of  $\text{Ca}_3\text{Ti}_2\text{O}_7$ . The experimental and simulated phonon DOS agree well overall, except for the phonon peak at  $\sim 87$  meV, which could indicate a limitation of the harmonic approximation used in our simulations, as the strong temperature-induced broadening of the 87 meV peak reveals a particularly strong anharmonicity of optical branches for the corresponding oxygen motions. Possible local relaxations around the Sr dopants in the experimental composition could also be at play. As one can observe, Ca atoms primarily occupy phonon energies up to 40 meV, while Ti atoms show a broad distribution of energies up to 80 meV. Since O anions form strong covalent bonds to Ti cations in the perovskite layer and are the lightest constituent atom, their vibrations cover the entire spectrum of energies. It is notable that, despite being slightly lighter than Ti, the Ca atoms vibrate at substantially lower frequencies. This reflects the strong covalent bond between Ti and O, while Ca ions in rock-salt layers maintain charge balance and stability [14]. Another interesting trend is that phonon frequencies show only a minimal degree of softening even at the highest temperatures measured (peak positions at 10 K are marked by vertical

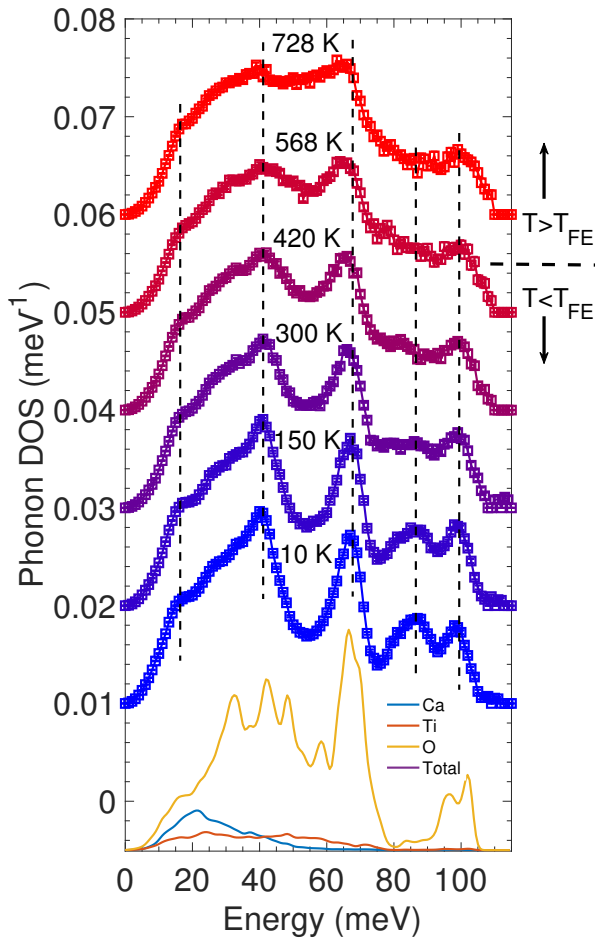


FIG. 7. Phonon density of states (DOS) of  $\text{Ca}_{2.1}\text{Sr}_{0.9}\text{Ti}_2\text{O}_7$  sample at multiple temperatures (indicated on top of each curve) across  $T_{FE} \sim 660$  K measured at the ARCS instrument with incident neutron energy  $E_i = 140$  meV. Experimental data is corrected for background, phonon occupation factor, and multiple and multiphonon scattering. On the bottom, DFT simulated neutron-weighted partial and total phonon DOS of  $\text{Ca}_3\text{Ti}_2\text{O}_7$  showing an excellent agreement. The area is normalized to one in each case. Curves are offset by 0.01 for clarity.

black dotted line for visualization). We further discuss the softening of Raman modes below.

### C. IXS measurements on single-crystal samples of $\text{Ca}_{3-x}\text{Sr}_x\text{Ti}_2\text{O}_7$ for $x = 0$ and $0.6$

We now discuss the phonon dispersions obtained from IXS. We note that IXS measurements were done on very small crystals  $\sim 0.5 \times 0.4 \times 0.06$  mm<sup>3</sup> and with beam size of  $0.035 \times 0.015$   $\mu\text{m}^2$ , allowing us to largely isolate a single crystalline grain. The Bragg peak intensities from any parasitic grains were three orders of magnitude weaker than those of the main crystal (ensuring any parasitic

inelastic signal was below the detection threshold). Figure 8 shows the phonon dispersions of low-energy modes in  $\text{Ca}_{2.4}\text{Sr}_{0.6}\text{Ti}_2\text{O}_7$  along several high-symmetry directions, below and above  $T_{FE} \sim 751$  K. Here, all high-symmetry directions refer to the low-temperature phase notation. The IXS spectra allow us to also extract the linewidth of acoustic phonons (when beyond the resolution limit, see Section II C for details). Error bars in all panels denote the measured phonon linewidths (half-width half-maximum on either side of the marker). The broadening of phonon linewidth on warming is evident for modes between 10 and 20 meV, consistent with INS measurements. For acoustic modes whose linewidth could be extracted (energies  $5 < E < 13$  meV along  $[H, 0, -10]$ ,  $[H, 4, 0]$ , and  $[2+H, 2-H, 0]$ ), the linewidth increases by a factor of 1.5 to 2 from 300 to 900 K.

The simulated phonon dispersions for  $\text{Ca}_3\text{Ti}_2\text{O}_7$  (grey curves in Fig. 8) agree well with the IXS results, especially for acoustic modes along high-symmetry directions. We do note, however, that our simulations resulted in weakly unstable modes (imaginary frequencies) of longitudinal acoustic modes propagating across layers ( $c$ -axis) for a small region near the Brillouin zone center. This could be an artefact from the limited supercell size used in our calculations ( $2 \times 2 \times 1$  supercell of the orthorhombic cell).

Using the IXS measurements, we can also selectively probe dynamics of in-plane rotation  $X_2^+$  and tilt  $X_3^-$ . Given the atomic displacement vectors of  $X_2^+$  distortion (Fig. 1c), the corresponding phonons can be measured along  $[H, 4, 0]$ . To note  $(-1, 4, 0)$  is a zone-boundary X point in the high-temperature phase, which becomes a zone-center  $\Gamma$  point in the low-temperature phase, and the intensity of the peak in the low-temperature phase primarily originates from the  $X_2^+$  distortion. Figure 8b shows the phonon dispersion along  $[H, 4, 0]$  at 80, 300, and 900 K. The phonon softening along the entire branch ranges from 0.25 to 0.85 meV between 300 and 900 K. For the same temperature range, the  $a$ -axis lattice parameter and the volume increase by 0.5% and 1.8%, respectively. The experimental Grüneisen parameter  $\gamma = -(V/E)(dE/dV)$  along  $[H, 4, 0]$  ranges from 4.4 at  $H = 0.1$  to 2.9 at  $H = 0.8$ , where  $V$  is the unit cell volume and  $E$  is the phonon energy at a given  $q$ . These  $\gamma$  values agree reasonably well with the simulated values in Ref. 14 near the zone-center, but differ close to the zone-boundary. However, the decreasing trend in  $\gamma$  from the zone-center to the zone-boundary is similar. It is important to note that quasi-harmonic simulations provide  $\gamma$  based on the volume change alone, while experimental data as function of temperature probe a thermal effective  $\gamma_{\text{th}}$ , which reflects intrinsic thermal anharmonic effects in addition to the effect of thermal expansion.

Similarly, for the atomic displacement pattern of  $X_3^-$  distortion (Fig. 1b), the corresponding phonons can be measured along  $[0, K, 10-3K]$  or  $[3-L, 0, 13-3L]$ . To note  $(0, 1, 7)$  and  $(3, 0, 13)$  are zone-boundary X points in the high-temperature phase, which become zone-center

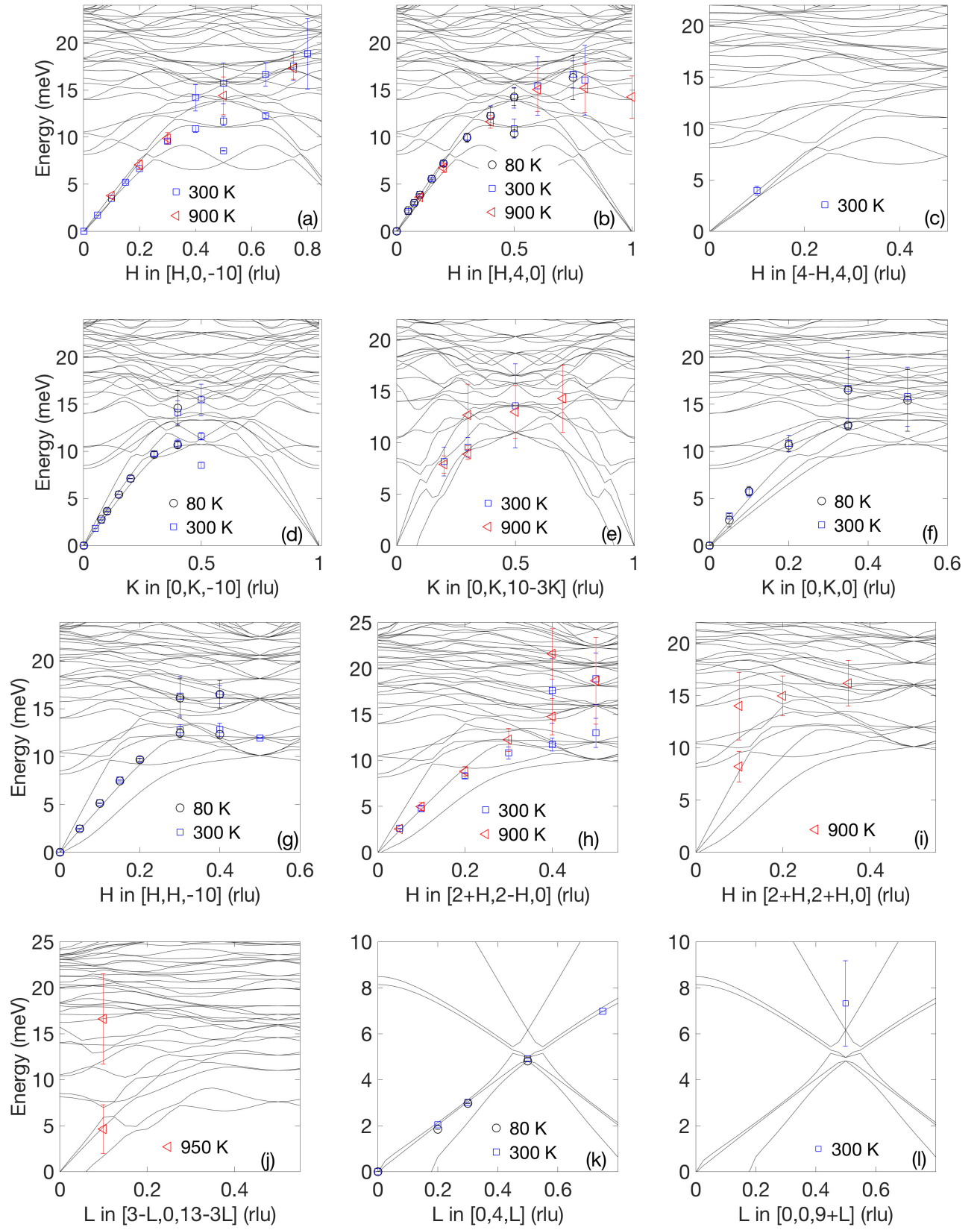


FIG. 8. Phonon dispersions of  $\text{Ca}_{2.4}\text{Sr}_{0.6}\text{Ti}_2\text{O}_7$  at multiple temperatures measured along different high symmetry directions below and above  $T_{FE} \sim 751$  K with HERIX. Error bars represent HWHM of the phonon linewidth on either side of the marker. Error bars in phonon energies from DHO fitting are smaller than the size of markers. Thin curves are the simulated phonon dispersions for  $\text{Ca}_3\text{Ti}_2\text{O}_7$ .

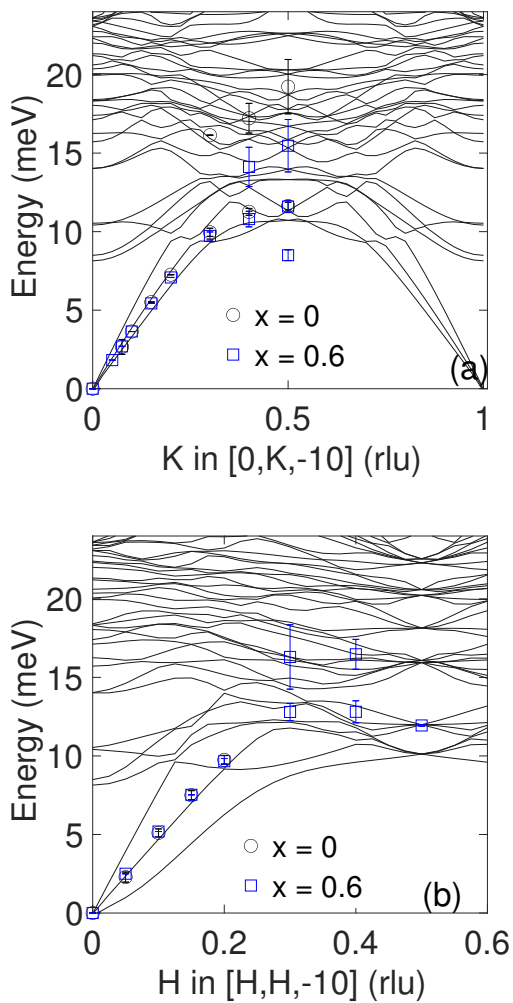


FIG. 9. Phonon dispersions of undoped ( $x = 0$ ) and doped ( $x = 0.6$ )  $\text{Ca}_{3-x}\text{Sr}_x\text{Ti}_2\text{O}_7$  at 300 K along different high symmetry directions measured with HERIX. Error bars represent HWHM of the phonon linewidth on either side of the marker. Error bars in phonon energies are smaller than the size of markers. Experimental markers are over-plotted on DFT simulated phonon dispersion of  $\text{Ca}_3\text{Ti}_2\text{O}_7$  showing an excellent agreement.

$\Gamma$  points in the low-temperature phase, and the intensity of both peaks in the low-temperature phase originates from  $X_3^-$  distortion alone. Figure 8(e,j) shows the phonon dispersion along  $[0, K, 10-3K]$  and  $[3-L, 0, 13-3L]$ . For the measured points, the phonon softening ranges from 0.3 to 0.7 meV between 300 and 900 K, the corresponding  $\gamma$  varies from 1.9 to 3.9. Here, we caution that the limited number of temperature points in IXS measurements limits detailed analysis of the phonon softening in both the high- and low-temperature phases independently. Our Raman scattering measurements will focus on this point (see below), although for  $\Gamma$  point modes only.

With our extensive IXS dataset, we can also comment on the quasi-2D character of  $\text{TA}_c^{[H00]}$  mode. This mode

was theoretically predicted to have a quadratic curvature similar to the ZA mode in 2D materials, and was found to be very sensitive to volume changes, with  $\gamma$  exceeding 25 near the zone-center [14]. Figure 8(a,d) shows the phonon dispersion along  $[H, 0, -10]$  and  $[0, K, -10]$ . Our IXS data do not show any appreciable quadratic curvature of  $\text{TA}_c^{[H00]}$  or  $\text{TA}_c^{[0K0]}$  branches. Our simulations along these same directions also do not reveal any significant curvature for long-wavelength TA branches. Huang *et al.* also obtained a quadratic curvature for the  $\text{TA}_c^{[HH0]}$  branch, albeit not as pronounced as for  $\text{TA}_c^{[H00]}$ . Our measurements of the  $\text{TA}_c^{[HH0]}$  branch, as shown in Fig. 8g, did not show any appreciable curvature. Since Sr doping on the Ca site (Ca ions in perovskite layer are preferably replaced as opposed to in the rock-salt layer [16, 37]) reduces the rotation and tilt to stabilize the structure because of significant size mismatch between two ions [10, 16, 37], it can potentially lead to changes in lattice dynamics. To understand the effects of doping on lattice dynamics, we also measured undoped  $\text{Ca}_3\text{Ti}_2\text{O}_7$  as shown in Fig. 9. Our measurements of acoustic modes along  $[0, K, -10]$  and  $[H, H, -10]$  for undoped  $\text{Ca}_3\text{Ti}_2\text{O}_7$  are essentially similar to those for on  $\text{Ca}_{2.4}\text{Sr}_{0.6}\text{Ti}_2\text{O}_7$ , but optic modes near the zone-boundary show significant drop in phonon energy of about 4 meV on doping. This is expected as acoustic modes involve atomic displacement of all atoms, and the mass ratio between undoped and doped samples is  $\sim 0.92$ . On the other hand, the observed optic modes involve the vibration of Ca/Sr atoms with a large mass difference ( $m_{\text{Sr}}/m_{\text{Ca}} = 2.2$ ), which along with a change in force-constants could potentially explain softening on doping. We also find that in our measurements,  $\gamma$  along  $[H, 0, -10]$  monotonically varied from -4.8 at  $H = 0.1$  to -1.7 at  $H = 0.3$ , which is also at odds with the large positive  $\gamma$  values obtained from the quasi-harmonic simulations [14]. But, again we stress the role of temperature effects. Nonetheless, with our IXS measurements, we can conclusively say that for the measured directions, phonons have 3D character.

#### D. Raman spectra on single-crystal $\text{Ca}_{2.4}\text{Sr}_{0.6}\text{Ti}_2\text{O}_7$ sample

We now focus on the detailed temperature dependence of Raman active modes at  $\Gamma$ . Figure 10a shows the Raman spectra measured between 294 and 1023 K on  $\text{Ca}_{2.4}\text{Sr}_{0.6}\text{Ti}_2\text{O}_7$ . Several of the phonon peaks disappear and new peaks appear upon heating above  $T_{FE} = 773$  K. From symmetry analysis, there are 69 Raman active modes [ $18A_1(xx, yy, zz) + 17A_2(xy) + 16B_1(xz) + 18B_2(yz)$ ] in the low-temperature phase, which reduces to 15 modes [ $4A_{1g}(xx, yy, zz) + B_{1g}(xx, yy) + 5E_g(xz, yz)$ ,  $E_g$  modes are doubly degenerate] in the high-temperature phase. The 69 Raman active modes and their powder averaged intensities are shown in our Raman scattering simulations in Fig. 11. The correspondence between measurements and simulations is indicated by denoting the

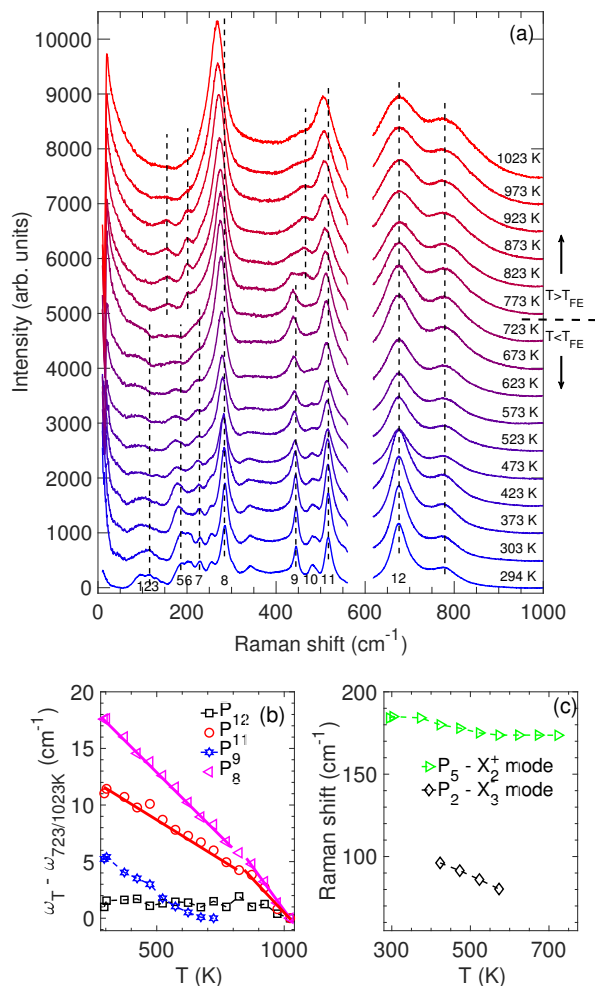


FIG. 10. (a) Temperature-dependent Raman spectra from  $\text{Ca}_{2.4}\text{Sr}_{0.6}\text{Ti}_2\text{O}_7$  single-crystal (measurement temperature indicated on each curve) across  $T_{FE} \sim 751$  K. The labels from 1 to 12 at the bottom refer to the mode eigenvectors shown in Fig. 11. Vertical dashed lines are guides to the eye showing the relative softening and broadening of the peaks below and above  $T_{FE}$ . Experimental data are corrected for the background. Curves are offset by 500 units for clarity. The gap from 561 to 617  $\text{cm}^{-1}$  is due to the data collections with different spectrometer position in the low and high Raman shift region. (b) Change in phonon frequency of selected peaks as a function of temperature across  $T_{FE}$ . (c) Temperature dependence of Raman shift of  $X_2^+$  and  $X_3^-$  modes below  $T_{FE}$ .

peak numbers. Similar to INS and IXS measurements, the phonon broadening is clearly visible in Raman spectra (Fig. 10) with increasing temperature. For example, in heating from 303 to 723 K in the low-temperature phase, peaks  $P_8$ ,  $P_9$ ,  $P_{11}$ , and  $P_{12}$  broaden by a factor of  $\sim 1.5$  to 2. Further heating in the high-temperature phase to 1023 K, peak broadening factor increases to  $\sim 2.5$  to 3. These values are consistent with measured broadening of acoustic modes using IXS measurements.

The temperature evolution of selected phonon peaks

(marked by black dashed line in Fig. 10a) is shown in Fig. 10(b,c). The eigenvectors corresponding to these phonons in the low-temperature phase are shown in Fig. 11. As one can observe, the phonon softening is quite small. The in-plane vibrating oxygen modes ( $P_8$  and  $P_{11}$ ) show modest phonon softening of around 11 to 18  $\text{cm}^{-1}$  ( $\sim 1.4$  to 2.2 meV), while oxygen atoms in the two perovskite layer vibrating towards ( $P_{12}$ ) or away ( $P_9$ ) from each other along the  $c$ -axis remain nearly rigid. Moreover, the rate of phonon softening on heating is enhanced in the high-temperature phase for peaks  $P_8$  and  $P_{11}$  as indicated by solid lines.

Our simulations also enable us to identify  $X_3^-$ ,  $X_2^+$ , and  $\Gamma_5^-$  modes. The peak  $P_2$  shows an overlap with  $X_3^-$  distortion, peaks  $P_5$  and  $P_6$  show an overlap with  $X_2^+$  distortion, and peaks  $P_3$  and  $P_4$  show an overlap with  $\Gamma_5^-$  distortion.  $P_3$  and  $P_4$  are fairly weak in both the experiments and simulations, and it is challenging to follow their temperature dependence. However, the temperature dependence of the relatively strong peaks  $P_2$  and  $P_5$  is shown in Fig. 10c. As one can observe, peak corresponding to the  $X_2^+$  distortion softens by  $\sim 10$   $\text{cm}^{-1}$  ( $\sim 1.2$  meV) in the low temperature phase from 294 to 723 K, while the  $X_3^-$  show pronounced softening of  $\sim 25$   $\text{cm}^{-1}$  ( $\sim 3$  meV) between 423 and 573 K, where its peak position can be extracted reliably. These conclusions are consistent with identification of the soft tilt and rigid rotation mode with neutron diffraction measurements on  $\text{Ca}_3\text{Mn}_{1.9}\text{Ti}_{0.1}\text{O}_7$  [11] and Raman measurements on  $\text{Ca}_3\text{Mn}_2\text{O}_7$  [12].

## V. SUMMARY

We have investigated the temperature dependence of the crystal structure and lattice dynamics using a combination of experiments and simulation. Our INS, IXS, and Raman scattering results reveal substantial broadening of phonons by a factor of 1.5 to 3 on heating from 10 to 1023 K. We find that rotational and oxygen breathing modes remain robust, while the tilt mode shows substantial phonon softening in the FE phase on heating. The rate of phonon softening on heating for in-plane polarized oxygen modes is enhanced in the high- $T$  paraelectric phase. The phonon dispersions from IXS do not show any significant upward curvature along the directions measured, for either undoped or doped compositions, which is at odds with a recent prediction of quasi-2D character for  $c$ -polarized TA modes propagating in-plane. In addition, our results for the Grüneisen parameter differ in both sign and magnitude from the previous simulations along certain directions, and highlight the need to explicitly include anharmonic contributions in calculation of thermodynamical properties such as thermal expansion and conductivity.

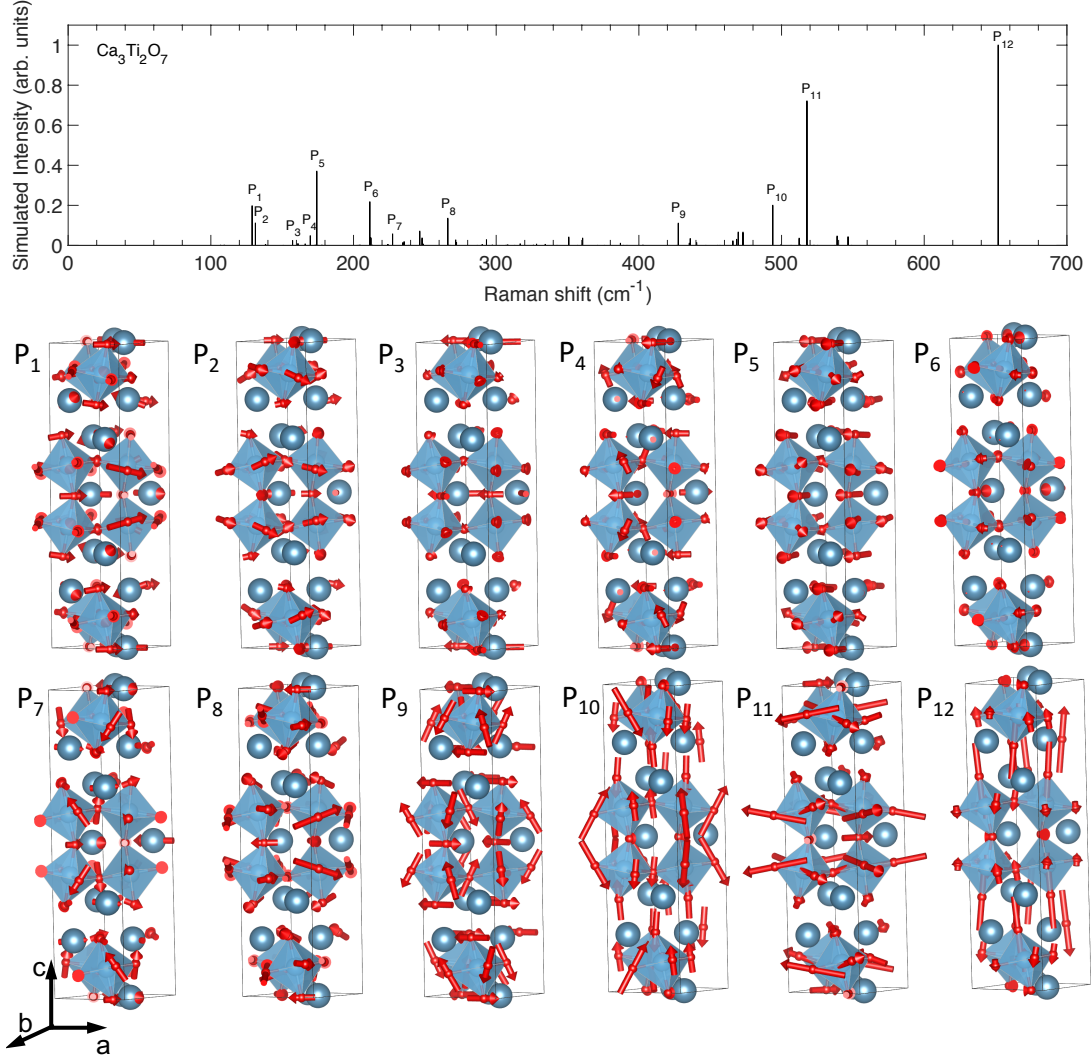


FIG. 11. DFT simulated phonon energy and corresponding powder averaged Raman intensity of all 69 Raman active modes of  $\text{Ca}_3\text{Ti}_2\text{O}_7$  below  $T_{FE}$ . Eigenvectors (normalized by square root of mass of the atoms) corresponding to the peaks marked in the top panel are also shown. The peak labelled  $P_2$  has an overlap with the high- $T$   $X_3^-$  distortion shown in Fig. 1. Similarly, peaks  $P_3$  and  $P_4$  have an overlap with the polar  $\Gamma_5^-$  distortion and peaks  $P_5$  and  $P_6$  have an overlap with the in-plane  $X_2^+$  distortion.

## VI. ACKNOWLEDGEMENTS

Neutron and x-ray scattering measurements, Raman spectroscopy, thermal characterization, and modeling (D.B., J.L.N, X.H., T.L.A., O.D.) were supported by the U.S. Department of Energy, Office of Science, Basic Energy Sciences, Materials Sciences and Engineering Division, through the Office of Science Early Career Research Program under Award No. DE-SC0016166. The work at Rutgers University was supported by the DOE under Grant No. DOE: DE-FG02-07ER46382. This research used resources of the Advanced Photon Source, a U.S. Department of Energy (DOE) Office of Science User Facility operated for the DOE Office of Science by

Argonne National Laboratory under Contract No. DE-AC02-06CH11357. The use of Oak Ridge National Laboratory's Spallation Neutron Source was sponsored by the Scientific User Facilities Division, Office of Basic Energy Sciences, U.S. DOE. Theoretical calculations were performed using resources of the National Energy Research Scientific Computing Center, a DOE Office of Science User Facility supported by the Office of Science of the US Department of Energy under contract no. DE-AC02-05CH11231.

## APPENDIX A

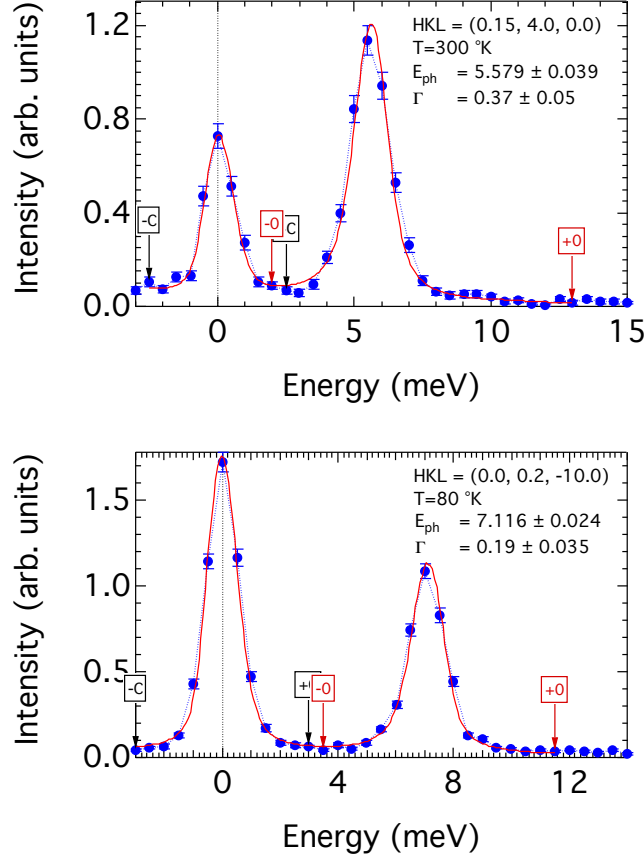


FIG. 12. Constant- $Q$  IXS spectra for the transverse acoustic mode at  $Q = (0.15, 4.0, 0)$  and  $(0.0, 0.2, -10)$  for  $\text{Ca}_{2.4}\text{Sr}_{0.6}\text{Ti}_2\text{O}_7$ . The lines are fits using a damped harmonic oscillator profile convoluted with the instrument resolution (see text). The values of  $E$  (in meV) and  $\Gamma$  (in meV) listed in the inset are the fitted phonon energy and phonon linewidth (corrected for resolution), respectively. Negative  $E$  corresponds to phonon annihilation and positive  $E$  corresponds to phonon creation.

- 
- [1] M. Fiebig, T. Lottermoder, D. Meier, and M. Trassin, *Nature Reviews Materials* **1**, 16046 (2016).
- [2] F.-T. Huang, F. Xue, B. Gao, L. Wang, X. Luo, W. Cai, X.-Z. Lu, J. Rondinelli, L. Chen, and S.-W. Cheong, *Nature Communications* **7**, 11602 (2016).
- [3] F.-T. Huang, B. Gao, J.-W. Kim, X. Luo, Y. Wang, M.-W. Chu, C.-K. Chang, H.-S. Sheu, and S.-W. Cheong, *NPJ Quantum Materials* **1**, 16017 (2016).
- [4] B. Gao, F.-T. Huang, Y. Wang, J.-W. Kim, L. Wang, S.-J. Lim, and S.-W. Cheong, *Applied Physics Letters* **110**, 222906 (2017).
- [5] F.-T. Huang and S.-W. Cheong, *Nature Reviews Materials* **2**, 17004 (2017).
- [6] N. A. Hill, *J. Phys. Chem. B* **104**, 6694 (2000).
- [7] J. Young, A. Stroppa, S. Picozzi, and J. M. Rondinelli, *J. Phys.: Condens. Matter* **27**, 283202 (2015).
- [8] S. Yoshida, K. Fujita, H. Akamatsu, O. Hernandez, A. Sen Gupta, F. G. Brown, H. Padmanabhan, A. S. Gibbs, T. Kuge, R. Tsuji, *et al.*, *Advanced Functional Materials* **28**, 1801856 (2018).
- [9] N. A. Benedek and C. J. Fennie, *Physical Review Letters* **106**, 107204 (2011).
- [10] Y. Oh, X. Luo, F.-T. Huang, Y. Wang, and S.-W. Cheong, *Nature Materials* **14**, 407 (2015).
- [11] F. Ye, J. Wang, J. Sheng, C. Hoffmann, T. Gu, H. Xiang, W. Tian, J. Molaison, A. dos Santos, M. Matsuda, B. Chakoumakos, J. Fernandez-Baca, X. Tong, B. Gao, J. Kim, and S.-W. Cheong, *Physical Review B* **97**, 041112(R) (2018).
- [12] A. Glamazda, D. Wulferding, P. Lemmens, B. Gao, S.-W. Cheong, and K.-Y. Choi, *Physical Review B* **97**, 094104 (2018).
- [13] H. Xiang, M. Guennou, J. Iniguez, J. Kreisel, and L. Bellaiche, *Physical Review B* **96**, 054102 (2017).
- [14] L.-F. Huang, X.-Z. Lu, and J. Rondinelli, *Physical Review Letters* **117**, 115901 (2016).
- [15] X. Liu, J. Wu, X. Shi, H. Zhao, H. Zhou, R. Qiu, W. Zhang, and X. Chen, *Applied Physics Letters* **106**, 202903 (2015).

- [16] G. Li, X. Liu, J. Lu, H. Zhu, and X. Chen, *Journal of Applied Physics* **123**, 014101 (2018).
- [17] M. Stone, J. Niedziela, D. Abernathy, L. DeBeer-Schmitt, G. Ehlers, O. Garlea, G. Granroth, M. Graves-Brook, A. Kolesnikov, A. Podlesnyak, and B. Winn, *Review of Scientific Instruments* **85**, 045113 (2014).
- [18] O. Arnold, J. C. Bilheux, J. M. Borreguero, A. Buts, S. I. Campbell, L. Chapon, M. Doucet, N. Draper, R. F. Leal, M. A. Gigg, V. E. Lynch, A. Markvardsen, D. J. Mikkelson, R. L. Mikkelson, R. Miller, K. Palmen, P. Parker, G. Passos, T. G. Perring, P. F. Peterson, S. Ren, M. A. Reuter, A. T. Savici, J. W. Taylor, R. J. Taylor, R. Tolchenov, W. Zhou, and J. Zikovsky, *Nuclear Instruments and Methods in Physics Research Section A: Accelerators, Spectrometers, Detectors and Associated Equipment* **764**, 156 (2014).
- [19] D. Bansal, C. Li, A. Said, D. Abernathy, J.-Q. Yan, and O. Delaire, *Physical Review B* **92**, 214301 (2015).
- [20] T. Toellner, A. Alatas, and A. Said, *Journal of Synchrotron Radiation* **18**, 605 (2011).
- [21] A. Said, H. Sinn, and R. Divan, *Journal of Synchrotron Radiation* **18**, 492 (2011).
- [22] J. Niedziela, D. Bansal, A. May, J. Ding, T.L.-Atkins, G. Ehlers, D. Abernathy, A. Said, and O. Delaire, *Nature Physics* **15**, 73 (2019).
- [23] S. Lovesey, *Theory of neutron scattering from condensed matter* (Clarendon Press, Oxford, 1984).
- [24] J. Thapa, B. Liu, S. Woodruff, B. Chorpeneing, and M. Buric, *Applied Optics* **56**, 8598 (2017).
- [25] G. Kresse and J. Hafner, *Physical Review B* **47**, 558 (1993).
- [26] G. Kresse and J. Furthmüller, *Physical Review B* **54**, 11169 (1996).
- [27] G. Kresse and J. Furthmüller, *Computational Materials Science* **6**, 15 (1996).
- [28] J. Perdew, A. Ruzsinszky, G. Csonka, O. Vydrov, G. Scuseria, L. Constantin, X. Zhou, and K. Burke, *Physical Review Letters* **100**, 136406 (2008).
- [29] A. A. Togo, F. Oba, and I. Tanaka, *Physical Review B* **78**, 134106 (2008).
- [30] S. Prosandeev, U. Waghmare, I. Levin, and J. Maslar, *Physical Review B* **71**, 214307 (2005).
- [31] L. Liang and V. Meunier, *Nanoscale* **6**, 5394 (2014).
- [32] N. A. Benedek, J. M. Rondinelli, H. Djani, P. Ghosez, and P. Lightfoot, *Dalton Transactions* **44**, 10543 (2015).
- [33] M. S. Senn, A. Bombardi, C. A. Murray, C. Vecchini, A. Scherillo, X. Luo, and S. W. Cheong, *Physical Review Letters* **114**, 035701 (2015).
- [34] M. Kratochvilova, F.-T. Huang, M.-T. F. Diaz, M. Klicpera, S. J. Day, S. P. Thompson, Y.-S. Oh, B. Gao, S.-W. Cheong, and J.-G. Park, *Journal of Applied Physics* **125**, 244102 (2019).
- [35] D. Orobengoa, C. Capillas, M. I. Aroyo, and J. M. Perez-Mato, *J. Appl. Cryst.* **A42**, 820 (2009).
- [36] A. Harris, *Physical Review B* **84**, 064116 (2011).
- [37] M. Elcombe, E. Kisi, K. Hawkins, T. White, P. Goodman, and S. Matheson, *Acta Crystallogr., Sect. B: Struct. Sci.* **47**, 305 (1991).